Available online at www.sciencedirect.com
ScienceDirect
International Journal of Heat and Fluid Flow 28 (2007) 1429–1442
International Journal of HEAT AND FLUID FLOW
www.elsevier.com/locate/ijhff

The low Reynolds number turbulent flow and mixing in a confined impinging jet reactor

Florian Schwertfirm [a], Johannes Gradl [b], Hans C. Schwarzer [c], Wolfgang Peukert [b], Michael Manhart [a,*]

[a] *Fachgebiet Hydromechanik, Technische Universität München, Arcisstr. 21, 80337 München, Germany*
[b] *Lehrstuhl für Feststoff- und Grenzflächenverfahrenstechnik, Friedrich-Alexander Universität Erlangen-Nürnberg, Cauerstr. 4, 91058 Erlangen, Germany*
[c] *Süd-Chemie AG, Waldheimer Str. 13, 83052 Bruckmühl, Germany*

Received 28 August 2006; received in revised form 16 April 2007; accepted 18 April 2007
Available online 18 June 2007

Abstract

Turbulent mixing takes an important role in chemical engineering, especially when the chemical reaction is fast compared to the mixing time. In this context a detailed knowledge of the flow field, the distribution of turbulent kinetic energy (TKE) and its dissipation rate is important, as these quantities are used for many mixing models. For this reason we conduct a direct numerical simulation (DNS) of a confined impinging jet reactor (CIJR) at $Re = 500$ and $Sc = 1$. The data is compared with particle image velocimetry (PIV) measurements and the basic flow features match between simulation and experiment. The DNS data is analysed and it is shown that the flow is dominated by a stable vortex in the main mixing duct. High intensities of turbulent kinetic energy and dissipation are found in the impingement zone which decrease rapidly towards the exit of the CIJR. In the whole CIJR the turbulence is not in equilibrium. The strong mixing in the impingement zone leads to a rapid development of a monomodal PDF. Due to the special properties of the flow field, a bimodal PDF is generated in cross-sections downstream the impingement zone, that slowly relaxes under relaminarising conditions. The time required for meso-mixing is dominating the overall mixing performance.

Keywords: Direct numerical simulation; Confined impinging jet reactor; Particle image velocimetry; Opposing jets; Turbulent mixing

1. Introduction

Turbulent mixing is of great importance in process engineering because it can considerably influence product properties (Baldyga and Bourne, 1999; Fox, 2003). When the chemical time scales t_R are in a similar range or faster than the turbulent time scales, the turbulent mixing determines the reaction rate and thus has a dominating influence on all subsequent steps as e.g. nucleation, growth, agglomeration, and aggregation in a precipitation process. Controlling the mixing process is therefore the key technology in process engineering of a wide class of products. When the chemical time scales are small, often confined impinging jet reactors (CIJR) or so-called opposed Tee-mixer configurations are used as they are capable of achieving rapid mixing. This configuration usually consists of two opposing feeding pipes or ducts opening in a main duct under different angles, leading to two impinging jets in a confined space. Speed and efficiency of the mixing in such a device are determined by the characteristics of the flow, e.g. the Reynolds number, the inflow conditions and the mixer geometry. By changing these process parameters the product properties might be adjusted to the desired values, e.g. the size and size distribution of particles in a precipitation process (Schwarzer et al., 2006).

In a general concept of mixing, three phases can be distinguished, namely (i) large scale mixing, (ii) meso-mixing,

* Corresponding author. Tel.: +498928922583; fax: +498928928332.
E-mail address: m.manhart@bv.tum.de (M. Manhart).

0142-727X/$ - see front matter © 2007 Elsevier Inc. All rights reserved.
doi:10.1016/j.ijheatfluidflow.2007.04.019

and (iii) molecular mixing (Baldyga and Bourne, 1999; Fox, 2003). While large scale mixing, sometimes referred to as macro-mixing, is determined by the large scale vortical motions of the turbulent flow field and the scalar integral scale (e.g. the initial conditions), meso-mixing is the process of reducing the scalar length scale down to the length scale range between the Kolmogorov and the Batchelor scale, the latter being determined by the Schmidt number. Molecular mixing or so-called micro-mixing is defined as the destruction of concentration fluctuations by molecular diffusion (Baldyga and Bourne, 1999). The large scale turbulent motions are a result of the large scale instabilities of the flow occurring in the specific geometry under specific flow conditions. Thus they are, along with the initial conditions of the scalar field, accessible to the designer of the mixer. The small scale motions are produced by the large scale motions in a cascade process, during which the individual characteristics of the large scales are mainly lost. Consequently, they are considered to assume a universal behaviour which is still assumed to be able to be described by the theory of isotropic turbulence (Kolmogorov, 1941). The total mixing time t_M is the total time required to reduce the initial spatial segregation of the reactants over the cascade of macro-mixing, meso-mixing, and micro-mixing down to a molecular segregation scale where the reactants can react. In CIJRs this mixing time is a function of the Reynolds number, inflow condition and mixer geometry, and represents the most important process parameter for the designer of the process.

In previous experimental studies on confined impinging jet reactors a dependence between the efficiency of mixing (e.g. t_M) and process parameters was constructed by applying a well defined chemical reaction (e.g. known t_R) as a "chemical ruler" and by measuring a certain quantity, e.g. the concentration of the product yield of the slow reaction in a competitive reaction system at the outflow (Johnson and Prud'homme, 2003). By relating the reaction time and the measured quantity with a timescale defined by the flow field, the mixing characteristics, and the process performance were derived. Most studies were confined to low and intermediate jet Reynolds numbers ($Re_j = 80$–600) and observed a plateau in mixing effectiveness at a certain Reynolds number (Tosun, 1987), above which on no further improvement in mixing effectiveness could be detected. Other researchers could not observe such a plateau. The reasons for this are still not clear, but as the local distribution of turbulent quantities and mixture fraction and the residence time of fluid particles in the specific flow regions are not known, certain flow effects or changes in flow features are hard to detect by considering global quantities only. Taking into account that the flow field is highly complex and dependent on the specific geometry, a global scaling may be difficult to develop in such a way. Nevertheless, experimental studies are still indispensable. A detailed and excellent summary on experimental studies of CIJRs can be found in Johnson and Prud'homme (2003). A qualitative impression of the flow field and mixing was given by Unger and Muzzio (1999). Unger and Muzzio conducted laser-induced flourescence (LIF) measurements and calculated the "intensity of segregation" over Re_j and presented pictures of instantaneous mixture fractions at several cross-sections, but could not provide quantitative measurements of the mixture fraction.

Roelands et al. (2003) studied the spatial distribution of the dissipation rate in a Y-mixer at a high inlet tube Reynolds number $Re = 9000$ numerically and found a strong variation of the spatial distribution of the dissipation rate and showed that zones of high dissipation rate do not necessarily overlap with zones where the fluid is macro-mixed. Liu and Fox (2006) present a CFD simulation with chemical reaction of the fast parallel reaction system studied experimentally by Johnson and Prud'homme (2003). The combination of a k–ϵ turbulence model with a DQMOM closure for the mixture fraction provides an acceptable agreement with the experimentally measured conversion at high Reynolds numbers and slow reactions. As the conversion is a global quantity, the local turbulence and concentration fields predicted by the simulation are not validated, as stated by the author, and the use of a k–ϵ model may be critical. According to Liu and Fox, there is still the need to validate approaches using standard turbulence models, especially at these low Reynolds numbers and taking into account that a strong three-dimensional flow with strong wall influence is considered. As present micro-mixing models rely on k and ϵ as an input, an accurate prediction of the flow field together with these quantities is essential.

Wood et al. (1991) performed the first direct numerical simulation (DNS) of the flow in a jet mixing head, a geometry similar to the CIJR considered here, and compared it with experimental data from LDA measurements. Their study was limited to jet Reynolds numbers $Re_j < 300$. They could detect the onset of oscillatory motions of the jets at $Re_j = 90$ and could not observe a stable impingement point position above $Re_j > 150$ in the experiments. Due to the prescription of laminar boundary conditions directly at the entry of the feeding pipes in the main mixing duct, this instability of the impingement point position could not be predicted in the simulations. However, a quantitative description of statistics of flow and scalar fields is missing. A DNS of a similar geometry was conducted by Telib et al. (2004). They could show that the flow field is fully turbulent inside the CIJR at a jet Reynolds number of $Re_j = 1270$, but did not see a symmetry break. As we will show in this study the symmetry break is an important feature which can be captured if the inlet pipes are included in the simulation.

As DNS became more available as a numerical experiment in recent years, there have also been numerous other numerical studies of opposing jets, e.g. Johansson and Andersson (2005). DNS of such flows can provide accurate and time-dependent data on basically all required quantities, such as turbulent kinetic energy k or dissipation rate ϵ and is therefore very useful for validating turbulence

and mixing models and for gaining insight into the physics of the flow. As the geometry in these simulations is not close to the geometry of the CIJR's, e.g. no strong confinement and the lack of any homogenous direction in the CIJR compared to Johansson and Andersson (2005), it is not possible to conclude from these simulations on the flow field or the mixing effectiveness of the CIJR. Nevertheless, some similarities between general impinging jet flow and the flow inside a CIJR can be expected, such as pronounced curvature effects and a local non-equilibrium between production and dissipation of turbulent kinetic energy.

In order to understand the mixing process in static flow mixers with complex geometries such as the CIJRs, a detailed knowledge of the local flow field, turbulence structure and mixture fraction is necessary. Additionally, this data can be used to validate and adjust turbulence models for such flows. For this purpose we performed a DNS of the flow field and mixing in a CIJR at a Reynolds number $Re = 500$ and a Schmidt number $Sc = 1$. The flow field is fully turbulent as previous studies in similar geometric configurations have shown (Telib et al., 2004). In the present study the feeding pipes of the CIJR are included in the computation to minimise the influence of the boundary conditions on the result. We performed PIV measurements of the flow in the same geometry and at the same Reynolds number and compare the first and second order statistics with this experimental data to validate the numerical results of the flow field. The basic flow features, which are profoundly different to non-confined jets are presented. Further, high order statistics are used to characterise the turbulent flow field inside the geometry and its influence on the mixing of a passive scalar. The mixing of the scalar is investigated in terms of first and second order statistics as well as with probability density functions (PDF's) at cross-sections of the T-mixer. Time scales for macro-mixing and micro-mixing are obtained and analysed.

The paper is structured as follows: in the second chapter the experimental and numerical methods are described in detail. In the third chapter, the first order moments of DNS and experiment are compared and the basic flow features are presented. A detailed discussion of the turbulent flow field with higher order statistics taken from the DNS is presented afterwards. In the final chapter, features of the scalar field and the mixing are presented and discussed using first and second order statistics as well as PDFs of the scalar within the cross-sections.

2. Experimental and numerical methods

2.1. Geometry and flow configuration

The basic geometry used for the study is shown in Fig. 1. It consists of two opposing feeding pipes with diameter D which open into a main duct at an angle of 90°, with quadratic cross-section and a sidelength of $0.5H = D$. The main duct is closed at one side and the feeding pipes are flush with this wall. The flow enters the mixer symmetrically via the feeding pipes, i.e. with the same Reynolds number, and leaves the mixer at the open side of the main mixing duct. The origin of the coordinate system is set at the intersection point of the symmetry axis of the feeding pipes with the symmetry axis of the main duct. The positive x-direction is defined to follow the flow down the main duct. The y-direction follows along the axis of the feeding pipes. The z axis is defined to close the right-hand side coordinate system. The flow Reynolds number is defined with the main duct width H and the bulk velocity u_b in the main duct $Re = u_b H/\nu$. This idealised geometry was modelled in the experiment and in the numerical simulation. In the following, this configuration of a CIJR will be referred to as T-mixer.

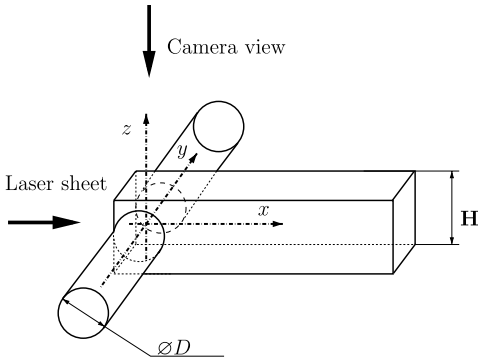

Fig. 1. The basic geometry configuration of the investigated CIJR with experimental setup.

2.2. Experimental setup

The mixer was built of two circular feeding tubes of $D = 40$ mm diameter and a length of $L_T = 1100\text{ mm} = 13.75H$ attached at the two opposite sides of a main channel that has a quadratic cross-section width $H = 80$ mm and a length of $L_D = 1000\text{ mm} = 12.5H$. The ends of the feeding tubes are flush mounted with the bottom of the main channel. At the entrance of the feeding tubes, lamellae are mounted which reduce undesired secondary motions in the oncoming flow. In order to ensure good visual conditions, the main duct is made of plexiglass with the exception of the aluminium edges for stabilising the apparatus. The fluid is provided by two 220 l feed casks located about 4 m above the top of the experimental setup. The hydrostatic pressure difference leads to a constant non-pulsating flow rate that is exactly adjusted by two flow control units. The temperature of the fluid in the casks is maintained at 25 ± 0.1 °C by thermostats, which is necessary to avoid natural convection in the main channel. At the outflow of the main channel, an overflow basin is installed, so that the outflowing fluid can be drained off in a controlled way. This configuration enables us to perform experiments at Reynolds numbers up to 1100 without measurable fluctuations in volume flux. The experiments

reported herein have been run at a bulk velocity in the main duct of $u_b = 6.25$ mm/s corresponding to $Re = u_b H/\nu = 500$.

For measuring the flow field, a 2D particle image velocimetry (PIV) technique was employed. The periphery of the PIV system (*Dantec Dynamics*) contains a Nd–Yag double pulsed laser (*Spectra Physics*) with a frequency of 10 Hz, two lenses for stretching and focusing the laser beam to a 1 mm thin sheet, a CCD camera (*80C42 Double Image 700/Dantec Dynamics*) with a Nikon AF Micro 60f/2.8D lens for recording images in a double frame mode. The evaluation system (*FlowMap 2.0-PIV-processor/Dantec Dynamics*) generated the final vector maps by a cross-correlation technique. Fig. 1 also shows the schematic experimental setup.

The maximum energy of the laser was 200 mJ and consequently, one pulse with a length of 10 ns has the theoretical power of 20 MW. The camera detecting the scattered laser light under an angle of 90° uses a CCD chip which includes 768×484 light-sensitive cells and the same number of storage cells. The CCD chip allows the recording of two different images, which are exposed by two consecutive laser pulses. Using these recorded double images as input for the cross-correlation technique, the quality of the vector plots depends on the time shift of the double image, which may not rise above a maximum, which is determined by the flow conditions and the desired spatial resolution. The evaluation of the cross-correlation was done on interrogation areas of 32×32 pixels which is a reasonable compromise between velocity dynamic range and spatial resolution. Thus, each singular measurement provides a 49×27 vector map by adjusting an overlapping of 50%, resulting in a spatial resolution of 1.63 mm. All vectors with an absolute value 10 times larger than the mean bulk velocity have been considered as invalid and replaced by a moving average. These replaced vectors appeared mainly at the wall regions, where reflections of the laser sheet were observed, but the number of invalid vectors was less than 3% of the total samples.

Polyamide seeding particles of a mean particle size of 20 μm and a density of 1020 kg/m^3 were used. In water of 25 °C, the sedimentation velocity of the seeding particles amounts to about 0.1% of the mean bulk velocity at a Reynolds number of 500. If the seeding particles follow the analysed slip-free fluid motion, it should be assured that the conducted measurements characterise the fluid flow field exclusively. Our tests demonstrated that a concentration of 15 mg/l provided the best results and was consequently used throughout the measurements. PIV measurements were conducted in four planes. Two lie in the symmetry plane spanned by the axis of the main and the feeding tubes at different x positions. The two other planes are displaced by $\pm 0.1875H$ from the symmetry plane in the z-direction in order to check the symmetry of the measured flow. We conducted two different kinds of measurements in order to check (i) the transient phase until statistical steadiness is reached and (ii) the mean flow at the statistical steady flow state. For the transient phase, every 5 s a single measurement was made. These measurements provide a complete time history of the transient running-in period. The statistical steady state was recorded by taking series of measurements after the 15 min of the complete transient period have elapsed. These series consist of 400 single measurements taken in bursts of three single measurements within one second followed by a break of 9 s. After 400 of such single measurements the whole system had to be shut down. This procedure has been repeated three times thus leading to 1200 single snapshots over a time period of 4000 s corresponding to $312.5H/u_b$.

2.3. Numerical method

For the DNS of the flow field the code MGLET is used (Manhart et al., 2001; Manhart, 2004). The incompressible Navier–Stokes equations, namely the conservation of mass

$$\frac{\partial u_i}{\partial x_i} = 0 \tag{1}$$

and momentum,

$$\frac{\partial u_i}{\partial t} + u_j \frac{\partial u_i}{\partial x_j} = -\frac{1}{\rho}\frac{\partial p}{\partial x_i} + \frac{\partial}{\partial x_j}\left(\nu\left(\frac{\partial u_i}{\partial x_j} + \frac{\partial u_j}{\partial x_i}\right)\right), \tag{2}$$

together with the passive scalar transport equation,

$$\frac{\partial c_\alpha}{\partial t} + u_i \frac{\partial c_\alpha}{\partial x_i} = \Gamma \frac{\partial^2 c_\alpha}{\partial x_j^2} \tag{3}$$

are solved in the finite volume (FV) formulation on a Cartesian grid, using a staggered variable arrangement (Harlow and Welsh, 1965). The discretisation in space and the approximation of the derivatives and the interpolation is accomplished by a second order central scheme. For the integration over time a third order Runge–Kutta method is used (Williamson, 1980). The incompressibility constraint is satisfied by solving the Poisson-equation for the pressure with an incomplete lower–upper (ILU) decomposition (Ferziger and Perić, 1997) and applying a correction step for the velocities and the pressure.

The geometry of the CIJR is represented in the numerical simulation by a main duct with square cross-section with a side length H and a length of $L_D = 4H$. Two circular feeding pipes intersect perpendicular and flush with the main duct at the bottom wall. The diameter of the feeding pipes is $0.5H$ and its length is $L_T = H$ (see Fig. 1). Compared to former simulations (see Telib et al., 2004) the geometry was extended to include the feeding pipes as it turned out that setting the inflow boundary condition directly at the entry plane of the feeding pipes in the main duct leads to a completely different flow field in the main duct.

This geometry is completely embedded in a regular Cartesian computational domain with the box size ($L_x = 4H, L_y = 3H, L_z = H$). The no-slip condition for

the velocities and zero-gradient condition for the scalar at the walls of the geometry were modelled by using the Immersed Boundary (IB) technique. In the IB technique, the node values of cells which are intersected by the geometry are not computed by solving the Navier–Stokes equations. Instead the values are interpolated with a high order scheme, so that the boundary condition is exactly fulfilled at the surface of the geometry. Cell values lying outside the flow field and inside the geometry are not computed. This method has been successfully used in various flow problems (Le Duc et al., 2005; Tremblay et al., 2001), for further details see (Peller et al., 2006).

At the outflow a zero-gradient and at the inflow planes of the feeding pipes laminar parabolic inflow profiles with peak inflow velocity V_0 are prescribed, as the Reynolds number in the feeding pipes is in the laminar regime. The scalar is set to $c(y/H=-1.5)=1.0$ and $c(y/H=1.5)=0.0$ at the inflow planes of the feeding pipes, leading to a maximal difference in mixture fraction of $\Delta c=1.0$, whereas the zero-gradient condition is set at the outflow.

The grid is chosen so that it resolves the wall friction and the Kolmogorov length scale in the flow field. The Kolmogorov length scale is defined as

$$\eta_K=\left(\frac{\nu^3}{\varepsilon}\right)^{1/4}. \tag{4}$$

In the region of intense mixing ($x/H\leqslant 1.51$) an equidistant grid with spacings of $(\Delta x,\Delta y,\Delta z)=(0.011H,0.005H,0.005H)$ is used. In this area, the grid spacing in x-direction is larger, because the main velocity gradients are in the y and z-direction. The grid spacing in the x-direction results in a distance of the first pressure point to the bottom wall of $x^+=1.55$. According to Johansson and Andersson (2005), the turbulence of the impinging jets in the stagnation point area is not in equilibrium, thus the Kolmogorov length scale is the lower limit of the resolution requirement. The grid is stretched from $1.51<x/H<3.75$ in the x-direction towards the outflow and from $y/H<-0.5$ and $y/H>0.5$ in the y-direction towards the inflow planes. This results in a grid consisting of 16.12×10^6 grid points of which 10.24×10^6 lie within the main duct of the T-mixer. The grid independence of the simulation was verified by comparing the Kolmogorov length scale of this simulation with the one computed on a finer grid. The fine grid had a grid spacing of $(\Delta x,\Delta y,\Delta z)=(0.007\overline{3}H,0.003\overline{3}H,0.003\overline{3}H)$ in the primary mixing zone ($x/H\leqslant 1.51$), e.g. it was refined by a factor of 1.5 in every direction, resulting in 40.32×10^6 grid points. The computation on the fine grid was initialised with an interpolated solution from the coarse grid. After the flow was fully developed, 1317 snapshots for statistical evaluation of the Kolmogorov length scale were taken, which is sufficient to compute the magnitude and the shape of the dissipation of TKE. On both grids, the Kolmogorov length scale distribution was identical except of statistical deviations and had its minimal size at $\eta_K=0.005H$ in the primary mixing zone, which is a indication that the coarse grid provides an adequate resolution of the flow considered.

3. Results

Both the experiment and the numerical simulation were carried out at a Reynolds number $Re=u_bH/\nu=500$. This corresponds to a jet Reynolds number with the bulk velocity at the exit of the feeding pipes of $Re_j=1270$. In the DNS, we took 9346 snapshots for statistical evaluation over a time span of $T_S=65.9H/u_b$. In the experiment, we were able to collect 1200 samples over a time span of $312.5H/u_b$. By comparing these two sample times it becomes evident that the dimensionless time in the numerical simulation is much shorter than in the experiment. The longer sample time in the experiment is a consequence of the low data rate of the PIV system. By comparing the samples taken from the 3 independently conducted realisations of the experiment we concluded that no low frequency dynamics were present in the flow. As will be shown, one feature of the flow is a break of the symmetry and a development of a large vortex in the main mixing duct due to the passing of the jets. This is seen in the experiment and in the numerical simulation. The direction of rotation is undetermined in the simulation as well as in the experiment, but once established it is stable for the rest of the experiment. In the numerical simulation only one continuous calculation was used for statistical sampling so only one sense of rotation was observed in the simulation. Several independent realisations of the experiment were conducted (due to the limited volume of the feeding casks) and thus different senses of rotation were observed. As the two flow conditions are related by reflections about the planes of the coordinate system (specific for each velocity component), all PIV measurements were transformed to the same sense of rotation as in the simulation before statistical averaging.

3.1. Numerical and experimental validation

For a verification of the DNS we compared the first and second order velocity statistics between the PIV measurements and the DNS. The data of the PIV measurements are limited to three x–y measurement planes at $z/H=0.0$ and $z/H=\pm0.1875$. In Fig. 2, the vector plots show that the global flow behaviour of the DNS is in accordance with the experiment. In the symmetry plane set up by the axes of the main and the feeding tubes (Fig. 2a), the u and v velocity components are symmetrical with respect to the x-axis. There is no pronounced stagnation point formed by the two opposing jets and consequently no jet in the core region of the main duct as found for example in investigations of similar flows (Telib et al., 2004). Instead, the main part of momentum of the feeding tubes is found in the offset planes at $z/H=\pm0.1875$ (Fig. 2b) and in the outer region of the main duct. The symmetry with respect to a reflection at the x–z plane is broken in the two offset planes, which indicates that a global vortex turning around the

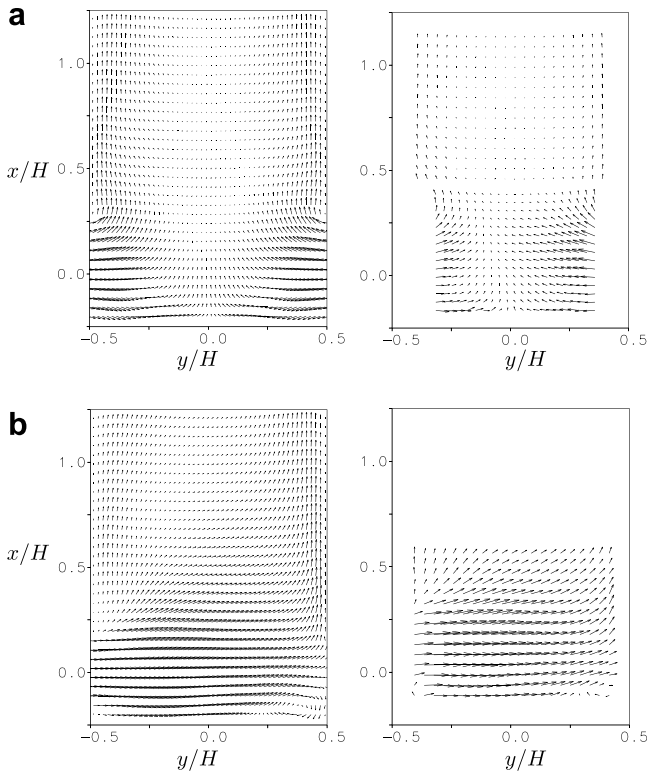

Fig. 2. Vector plots of the mean flow field at $z = 0.0$ (a), $z = 0.1875H$ (b); DNS left, experiment right column.

x-axis has developed. The fact that this can be observed in the experiment as well as in the DNS underlines that the symmetry breaking is an inherent feature of this flow. It has to be noted here that in the DNS this feature cannot be found if the feeding tubes are not simulated as a whole but rather approximated by boundary conditions set directly at the entrance of the feeding tubes to the main duct as e.g. in the investigation of Telib et al. (2004) and Wood et al. (1991).

Quantitative comparisons between experimental and numerical results are given in Fig. 3 for the time averaged flow and in Fig. 4 for the root mean square of the measured velocity components. The gross features of the mean profiles and root mean square profiles agree between experiment and DNS, although there are some unexpected quantitative differences. The main difference in the time averaged flow fields is found close to the bottom wall of the main duct. In this region, the main duct's axial velocity component u is higher in the simulation as can be seen in the profile along the axis of the feeding pipes (Fig. 3a). Moreover, the predicted main duct's velocity component v is higher in the offset planes at $z/H = \pm 0.1875$ and $x/H < 0.2$. This means that the momentum of the feeding streams, as shown by the high values at $x < 0.2$, is directed somewhat more to the bottom wall in the DNS than in the experiment which leads to the observed differences. The distribution and intensities of the velocity fluctuations in Fig. 4 display a good agreement. The differences in the u_{rms} component (Fig. 4a) and in the location of the maxima in (Fig. 4b) originate in the differences of the mean velocity field.

The study of the grid resolution showed that the simulation is fully resolved. Therefore, a reason for the deviations may be found in the inflow conditions which are difficult to match exactly between experiment and DNS. To check for the influence of the length of the feeding pipe on the simulation, we conducted another simulation with a length of the feeding pipes of $L_{\mathrm{T}} = 2.0H$. The comparison of the mean flow fields showed that the direction of the momentum of the feeding streams changes slightly and the mean flow fields are closer to the experimental results. A noticeable difference between simulation and experiment still remains, which may be due to the inflow conditions in the experiment. Although the flow in the feeding pipes is laminar (jet Reynolds number $Re_{\mathrm{j}} = 1270$), it cannot be definitely excluded in the experiment that there are some disturbances which originate from the feeding pipes and influence the development of the flow structure in the main duct.

Additionally, Figs. 3b and 4b demonstrate the symmetry of the flow. The differences in the curves at $z/H = \pm 0.1875$ are small. This shows that the statistics can be regarded as

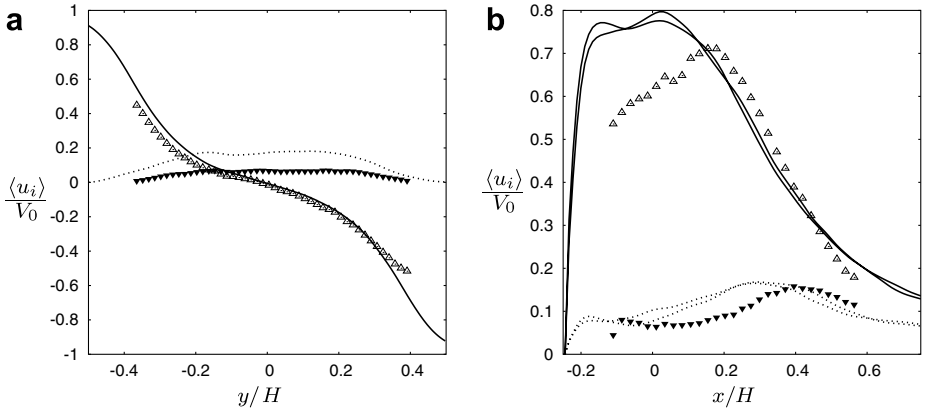

Fig. 3. (a) Mean velocity profiles over the axis of the feeding pipes ($x/H = 0.0, z/H = 0.0$); (b) absolute values of the mean velocity over the main duct ($y/H = 0.0, z/H = \pm 0.1875$); $\langle v\rangle/V_0$ (solid) and $\langle u\rangle/V_0$ (dot) from DNS, $\langle v\rangle/V_0$ (phantom triangle) and $\langle u\rangle/V_0$ (solid triangle) from experiment.

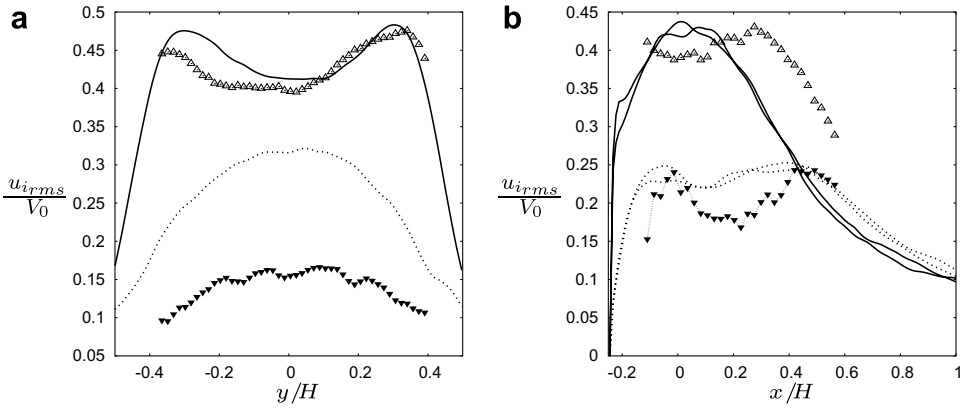

Fig. 4. (a) rms velocity profiles over the axis of the feeding pipes ($x/H = 0.0, z/H = 0.0$); (b) rms velocity profiles over the main duct ($y/H = 0.0$, $z/H = \pm 0.1875$); v_{rms}/V_0 (solid) and u_{rms}/V_0 (dot) from DNS, v_{rms}/V_0 (phantom triangle) and u_{rms}/V_0 (solid triangle) from experiment.

converged and that following symmetry properties are present:

$$\begin{pmatrix} u(x,y,z) \\ v(x,y,z) \\ w(x,y,z) \end{pmatrix} = \begin{pmatrix} u(x,-y,-z) \\ -v(x,-y,-z) \\ -w(x,-y,-z) \end{pmatrix}. \quad (5)$$

3.2. Flow field and turbulence

In the following, we present a detailed discussion of the mean flow field, the structure of the turbulence, and the mixing of a passive scalar obtained by the DNS. The symmetry property is used for the averaged data presented in the subsequent plots in order to double the available statistical samples, except for Figs. 2 and 6.

3.2.1. Time averaged flow fields

The time averaged flow field is best visualised by vector plots of the mean velocities in planes normal to the x-direction (Fig. 5). The generic symmetry of the mixer is broken as the two inflow jets pass each other and impinge on the opposite wall. This 'passing' of the jets gives rise to a large helical vortex, in the following called 'main vortex', which fills the whole mixer. Four additional features are visible at $x/H = 0.0$: (1) a strong shear layer forms between the to inflow jets, (2) a secondary vortex evolves in the corner

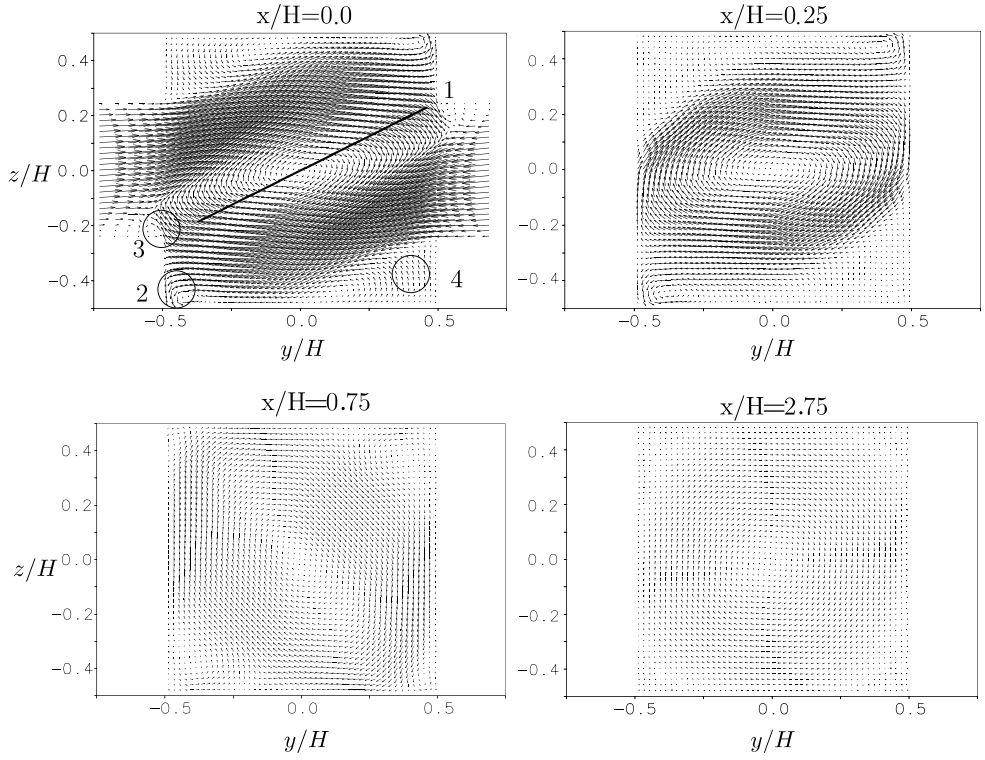

Fig. 5. Vector plots of the mean flow field at $x = 0H$, $x = 0.25H$, $x = 0.75H$ and $x = 2.75H$.

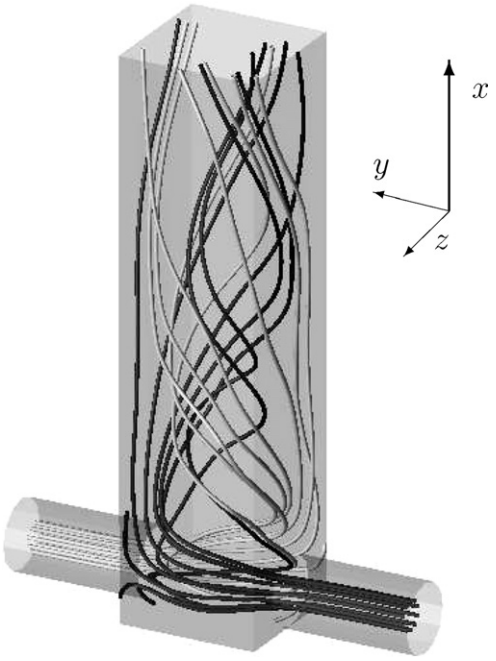

Fig. 6. Streamlines of the mean flow field.

where the jets impinge on the wall, (3) there is back flow into the feeding pipes, and (4) there are large regions of relatively small mean velocities where also secondary vortices evolve. When following the x-axis, the main vortex develops towards axisymmetry with respect to the x-axis, giving rise to secondary vortices at $x/H = 0.75$ in each corner of the main duct and finally being almost axisymmetric at $x/H = 2.75$. As the streamlines in Fig. 6 show, the rotational energy is strong enough to give rise to one rotation around the x-axis within the computational domain. The streamwise velocity is small in the vortex core and even slightly negative between $0.25 \leqslant x/H \leqslant 1.25$.

3.2.2. Second order statistics

The velocity fluctuations are defined by $u_{i,\mathrm{rms}} = \langle u_i'^2 \rangle^{1/2}$ with $u_i' = u_i - \langle u_i \rangle$ and the turbulent kinetic energy (TKE) by $k = \frac{1}{2}(u_{\mathrm{rms}}^2 + v_{\mathrm{rms}}^2 + w_{\mathrm{rms}}^2)$. Fig. 7 shows the distribution of the TKE at three different slices normal to the x-axis ($x/H = 0.0$, 0.25 and 0.75) and normalised by the kinetic energy of the peak inflow velocity $1/2V_0^2$. The two jets are deflected and high intensities of TKE are found at the shear layers at the edges of the jets. As the shear in between the two opposing jets is stronger than on the edges, the highest levels of the turbulent kinetic energy are found in the region where the jets pass each other (Fig. 7, $x/H = 0.0$). However, the distribution cannot be compared to that of a classical mixing layer, in which the root-mean-squares of all three velocity components peak in the centre of the mixing layer (see e.g. Pope, 2000). In our case, we do not find a peak in the centre between the two streams. Instead, there are two peaks in the distribution of the turbulent kinetic energy shifted away from the centre. The peak intensity of the TKE is two times higher in the present case than in a classical mixing layer with a velocity difference of $2V_0$. Further downstream at $x/H = 0.25$, which is still at the edge of the feeding pipes, the turbulent kinetic energy is already 25% lower but has a similar spatial distribution, slightly shifted according to the rotation of the jets around the x-axis as they move downstream. At $x/H = 0.75$, however, the peaks have moved to the outer region of the main duct and the intensity is 75% lower than the maximum intensity at $x/H = 0.0$. The peaks are located in the main streams which are visible

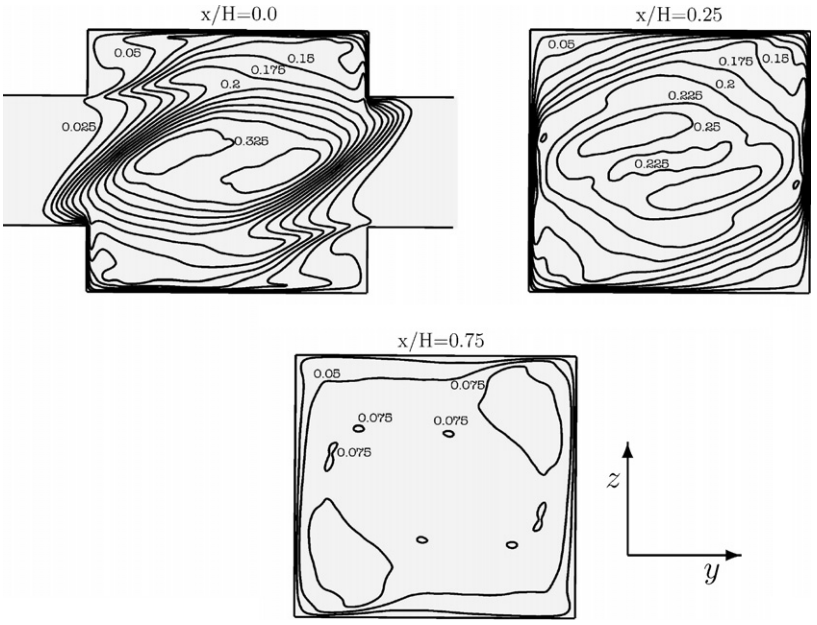

Fig. 7. Isolines of the turbulent kinetic energy $k/0.5V_0^2$.

in Fig. 6. The largest contribution to the TKE is due to the v velocity fluctuations. The fluctuation intensities in the u- and w component are at about 40–50% of the intensity of the v fluctuation (not shown here).

3.2.3. Production and dissipation of turbulent kinetic energy

In the statistical steady flow inside the T-mixer, the mean turbulent kinetic energy is constant over time. It is produced via the term

$$P_k = -\left\langle u_i' u_j' \right\rangle \frac{\partial \langle u_i \rangle}{\partial x_j}, \tag{6}$$

and dissipated via the term

$$\epsilon = 2\nu \left\langle \frac{\partial u_i'}{\partial x_j} \frac{\partial u_j'}{\partial x_i} \right\rangle. \tag{7}$$

Positive values of the production term stand for the extraction of energy from the mean flow and feeding the turbulence, while negative values represent the contrary. The dissipation is always positive and appears with a negative sign in the balance equation for the turbulent kinetic energy, thus always removes turbulent kinetic energy towards inner energy. Additionally molecular and turbulent transport processes distribute the TKE in space. In Fig. 8 the production and dissipation, normalised by V_0^3/H, are shown in the plane at $x/H = 0.0$. The production is high at the shear layers on the sides of the deflected jets as well as in the zones of backflow into the feeding pipe. TKE is predominately produced by fluctuations in the v component. The gradient of the v component in z-direction leads to a turbulence production by the term $-\langle v'w' \rangle \partial \langle v \rangle / \partial z$ and the gradient in the y-direction which is due to the strong deceleration of the jets is effective via the term $-\langle v'v' \rangle \partial \langle v \rangle / \partial y$. Directly at the wall where the deflected jets impinge production is negative. The highest values of the dissipation are found at the walls, especially in the region where the jets impinge, and in the backflow zone in the feeding pipes. Remote from the walls there are also regions of high dissipation at the shear layers of the jets and a broad plateau around the stagnation region. As in similar flows (Johansson and Andersson, 2005) the turbulence around the stagnation region is far from equilibrium, and the production exceeds the dissipation in the plane shown. In the region where the jets pass, it is 15 times higher and when considering the absolute peak values, the production is still higher by a factor of 4. In Fig. 9a, the production and dissipation of TKE are shown along the centreline of the main duct. In addition, both quantities are averaged over (y, z) cross-sections by the following operation

$$\tilde{\Phi}(x) = \frac{1}{H^2} \int_{-0.5}^{+0.5H} \int_{-0.5H}^{0.5H} \Phi(x)\, \mathrm{d}y\, \mathrm{d}z \tag{8}$$

and plotted over the x-axis of the T-mixer (symbols). In the impingement zone the cross-sectional average of produc-

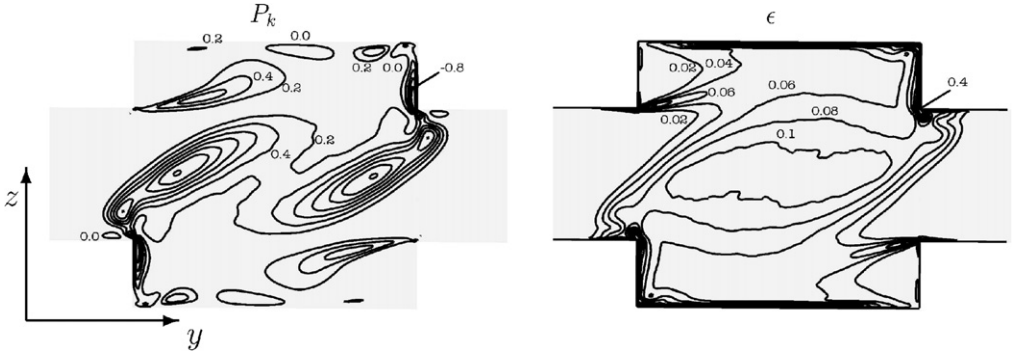

Fig. 8. Isolines of production P_k and dissipation ϵ of turbulent kinetic energy at $x/H = 0.0$, normalised with V_0^3/H.

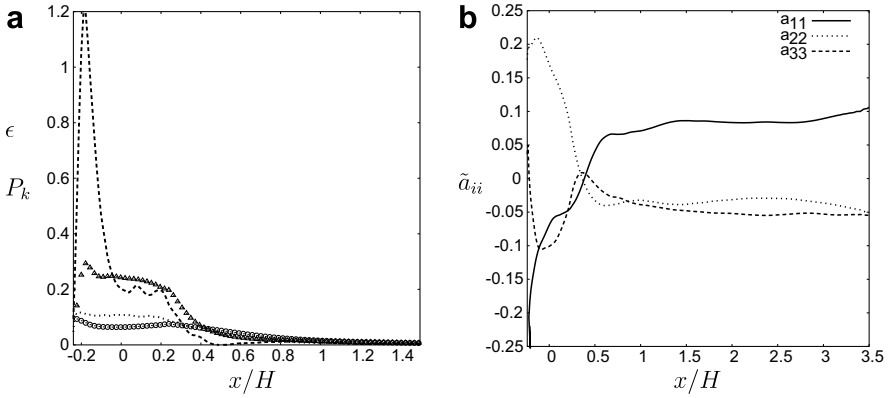

Fig. 9. (a) Production P_k (triangle) and dissipation ϵ (circle) of turbulent kinetic energy averaged over cross-sections; production P_k (dashed) and dissipation ϵ (dots) along the centreline of the main duct; (b) components of the trace of the anisotropy tensor over the main duct; averaged over cross-sections excluding wall layer.

tion exceeds the mean dissipation by a factor of approximately 3.8, at the centreline even by a factor of 10. Above $x/H > 0.5$, the dissipation exceeds the production, beginning with a clear surplus between $0.5 < x/H < 1.0$ and then leveling to a constant excess of dissipation to production by a factor of approx. 2 towards the end of the mixing duct. In the whole mixer no equilibrium in the balance of the TKE exists. Due to the low Reynolds number, turbulence is not sustained in the main duct, and thus the dissipation is higher than the production.

3.2.4. Turbulence structure

To characterise the turbulence in the static mixer, the anisotropy tensor according to Lumley (Lumley and Newman, 1977) is used:

$$a_{ij} = \frac{\overline{u_i' u_j'}}{\overline{u_k' u_k'}} - \frac{1}{3}\delta_{ij}. \tag{9}$$

In Fig. 9b the components of the trace $i = j$ of the anisotropy tensor, which correspond to the normalised turbulent kinetic energy, are plotted over the x-axis. The components have been averaged over cross-sections with operation (8). In the region $x/H \leqslant 0.25$ the turbulence is highly anisotropic and dominated by the v component. In the small region between $0.25 < x/H < 0.75$, the turbulent kinetic energy is being redistributed almost equally among the three components. Further downstream the duct the contributions of the a_{22} and a_{33} components are reduced, whereas a_{11} increases and stays almost constant from $x/H > 0.75$ on. As mentioned before, the main vortex is slowly developing towards axisymmetry, and due to the small Reynolds number in the main duct the flow tends to a laminar state.

Based on theses observations we distinguish between three different zones in the mixer: (a) mixing zone ($x/H \leqslant 0.25$), (b) isotropic zone ($0.25 < x/H \leqslant 0.75$), and (c) relaminarisation zone ($x/H > 0.75$).

The mixing zone ($x/H = 0.0$) is highly turbulent, the turbulent kinetic energy (Fig. 7) has its highest values, and the velocity fluctuations in the v component are considerably higher than the fluctuations in the u and w component. In the isotropic region, all three components have a similar amplitude with somewhat decreased TKE intensities compared to the mixing region. In the relaminarisation zone, the turbulence level decreases constantly as the Reynolds number in the main duct of $Re_b = u_b H/\nu = 500$ is not high enough to sustain turbulence. Here, the main vortex is the dominant feature and the anisotropy of the flow rises again.

3.3. Scalar field and mixing

3.3.1. Time averaged scalar fields and scalar variance

The structures of the jets and the main vortex are also visible in the mean scalar field (Fig. 10). Due to the 'passing' of the jets, relatively unmixed fluid is transported to the opposite wall and even enters the opposite feeding pipe at one edge of the jets. At the other edge of the jets, strong gradients in the mean field appear (Fig. 10, $x/H = 0.0$). When moving down the main duct, the rotational character of the flow causes the structure of the mean concentration field to rotate clockwise, while slowly approaching a state of homogeneous mean concentration (Fig. 10, $x/H =$ 0.25, and 1.25, respectively). The highest values of the scalar variance are found at the edges of the jets where fluid from the opposing jet enters the feeding pipe (Fig. 11, $x/H = 0.0$). At the opposite boundaries of the jets, the concentration fluctuations are considerably lower. Again the rotational character of the flow is clearly visible. When moving downstream, the two regions of high fluctuation intensities rotate clockwise and decrease in amplitude

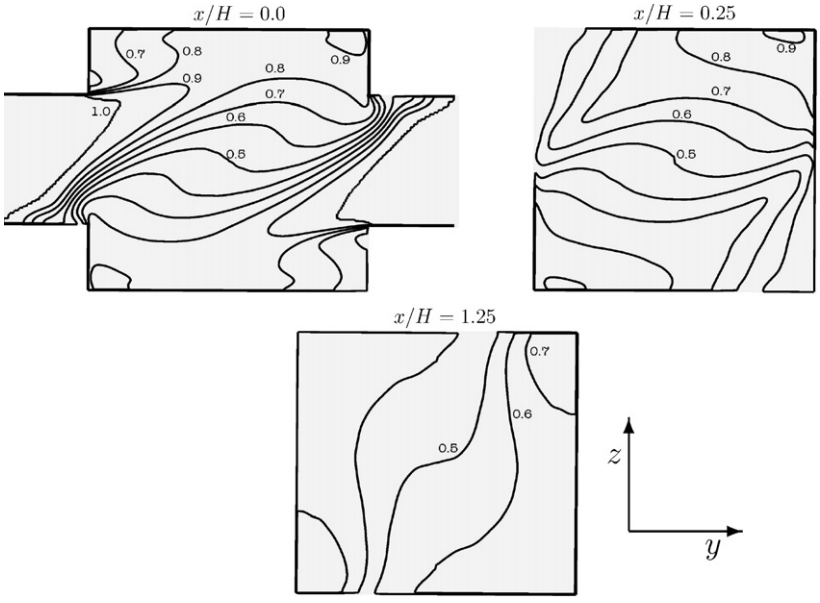

Fig. 10. Isolines of the mean scalar field $\langle c \rangle / \Delta c$, normalised by initial scalar difference.

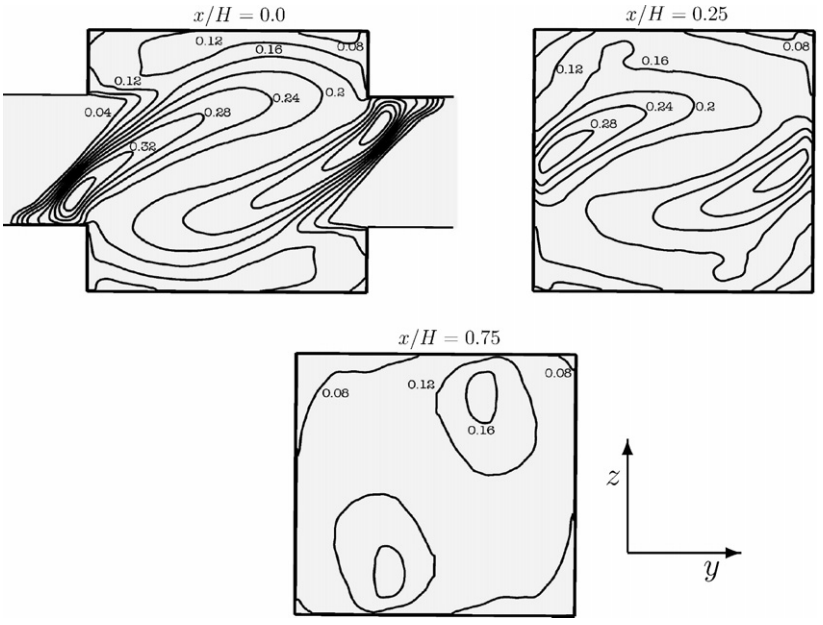

Fig. 11. Isolines of the rms of the scalar field $\langle c'c' \rangle^{1/2}/\Delta c$, normalised with initial scalar difference.

(Fig. 11, $x/H = 0.25$, and $x/H = 0.75$). These regions of high fluctuation intensities correspond with the cores of the two jets (compare Figs. 6 and 7, $x/H = 0.75$).

3.3.2. Mixing time scales

In the process of mixing the scalar traverses from the unmixed state to the fully mixed state ($c = 0.5$). In an Eulerian frame one can define a large scale variance (LSV) as the deviation of the local mean to the fully mixed state $\xi'^2 = (\langle c \rangle - 0.5)^2$ (Liu and Fox, 2006; Fox, 2003) and a small scale variance (SSV) as the local fluctuation of the concentration around its local mean $\langle c'^2 \rangle$. The small scale variance transport equation is given by:

$$\frac{\mathrm{D}\langle c'^2\rangle}{\mathrm{D}t} = -2\langle c'u_j'\rangle\frac{\partial\langle c\rangle}{\partial x_j} - 2\Gamma\left\langle\left(\frac{\partial c'}{\partial x_j}\right)^2\right\rangle + \Gamma\frac{\partial^2\langle c'^2\rangle}{\partial x_j^2} - \frac{\partial\left\langle u_j' c'^2\right\rangle}{\partial x_j}. \tag{10}$$

The first term on the right-hand side is usually larger than zero (Kawamura et al., 1998; Johansson and Wikström, 1999) and hence called production term P_c. The second term is the dissipation term ϵ_c, which is always negative. The last two terms represent the molecular and turbulent diffusion, respectively. The production term also appears in the transport equation for the LSV but with opposite sign. This implies that this term is responsible for removing LSV (as the molecular dissipation in the LSV transport equation is negligible). The reduction of LSV via the term P_c is sometimes referred to as macro-mixing or meso-mixing while the dissipation of SSV is referred to as micro-mixing. In (Fig. 12), the production P_c and dissipation ϵ_c of the small scale scalar variance are shown at $x/H = 0.0$. They are large at the inner edges of the jets, which indicates intense macro-mixing and micro-mixing. However, there are large zones where P_c is negative (dark grey). In these zones, primarily where the jets impinge at the opposite walls close to the feeding pipes, LSV is increased and SSS is reduced by this term. This is the result of counter gradient turbulent transport. The dissipation of SSV is always negative. To compare the importance of large and small scale mixing, time scales have been introduced (Fox, 2003). The large scale mixing time is

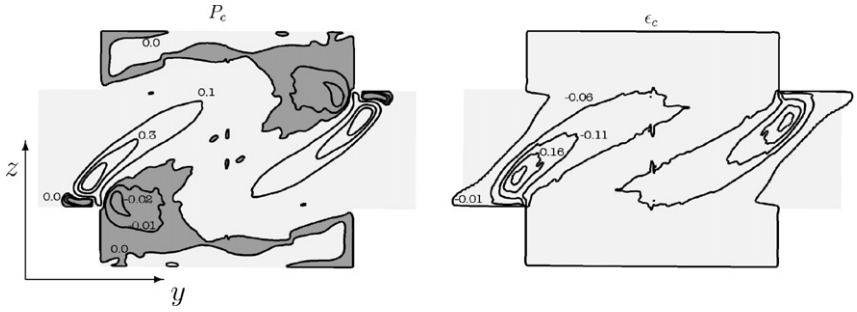

Fig. 12. Isolines of production P_c and dissipation ϵ_c of scalar variance at $x/H = 0.0$, normalised with $\Delta c^2 V_0/H$. Dark grey indicates zones of negative production.

$$t_{\mathrm{LS}} = \frac{\langle \xi'^2 \rangle}{-2\langle u_j' c' \rangle \frac{\partial \langle c \rangle}{\partial x_j}} \tag{11}$$

and the small scale mixing time is

$$t_{\mathrm{SS}} = \frac{\langle c'^2 \rangle}{2\Gamma \left\langle \left(\frac{\partial c'}{\partial x_j} \right)^2 \right\rangle}. \tag{12}$$

Both times are defined by the ratio of the respective quantity to its sink term, e.g. SSV to its dissipation rate. While t_{SS} is well defined everywhere in this flow, t_{LS} would become negative and even infinite where $P_c \to 0$. It is obvious that a definition of large scale mixing time on a local basis is not suitable for this complex flow. However, on an integral scale the LSV must decrease when following the main stream direction. For this reason, we compare the mixing times t_{LS} and t_{SS} calculated from the cross-sectional averages of the quantities along the main duct in Fig. 13. Both mixing times have their lowest values in the impingement zones and increase along the course of the main mixing duct. From $x/H > 3$ on, t_{LS} decreases again towards the outflow. Generally, t_{SS} is lower than t_{LS}, and thus the large scale mixing is the dominant process controlling the mixing performance of this configuration. It should be noted that this statement holds only for the Schmidt number of unity considered in this paper.

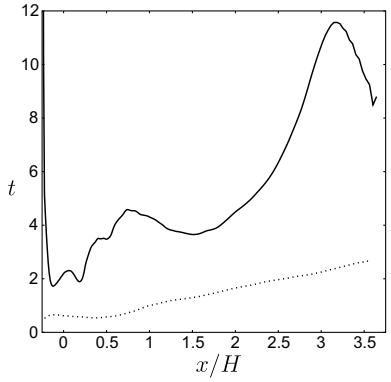

Fig. 13. Mixing time scales calculated from cross-sectional averages: t_{LS} (solid) and t_{SS} (dots).

3.3.3. PDF of the scalar distribution

As a result of the complex 3D structure, we characterise the total mixing process by referring to the probability density functions (PDF) $f(\Psi)$ of the concentration fields in different cross-sections, where Ψ is the sample-space variable corresponding to the normalised concentration $c/\Delta c$. The PDFs, which are shown in (Fig. 14), are constructed from 20 instantaneous concentration fields for slices normal to the x-axis, and therefore characterise the concentration distributions in the specific slices. In (Fig. 15) the corresponding variances $\Xi'^2 = \int (c - 0.5)^2 f(\Psi)\,\mathrm{d}\Psi$ of the cross-sectional PDFs are shown (solid). It is to be noted that the variance of the PDF is the sum of the cross-sectional average of small scale (SSV) and large scale (LSV) variance. At $x/H = 0.0$, a typical bimodal PDF is observed which is due to the two streams of unmixed fluid entering the mixing region by the feeding pipes. This is the position at which the absolute variance has its maximum. From $x/H = 0.0$ to $x/H = 0.75$ intense mixing takes place that reduces the variance of the PDF. At $x/H = 0.75$ the peak of the PDF has moved to the mean concentration $c/\Delta c = 0.5$ with tails of the PDF still reaching to the unmixed concentration values. The change of the PDF's shape within the cross-sections between $x/H = 0.0$ and $x/H = 0.75$ is a result of rapid mixing in this region (i.e. the mixing and the isotropic region), but still almost completely unmixed patches of fluid are present at $x/H = 0.75$ that are removed in the subsequent development until $x/H = 3.75$. However, between $x/H = 1.25$ and $x/H = 2.75$ the probability of the fully mixed state decreases unexpectedly. The PDF changes to a bimodal distribution. It should be noted that this change coincides with a decrease of the variance along the x-axis (Fig. 15, solid line). Accordingly with the PDFs in (Fig. 14) the variance has its maximum at the feeding pipes' inlet ($x/H = 0.0$). There is a rapid decrease until $x/H = 0.75$ after which the variance decreases slowly. The same ten-

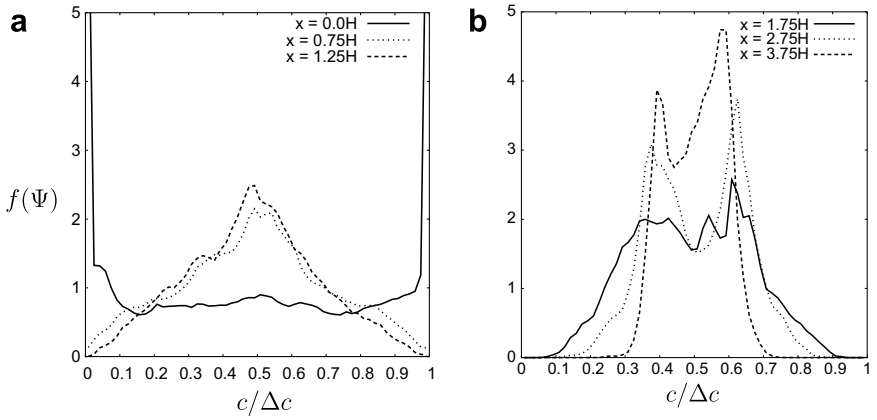

Fig. 14. PDF $f(C)$ of the concentration distribution at different cross-sections (calculated from 20 independent scalar fields).

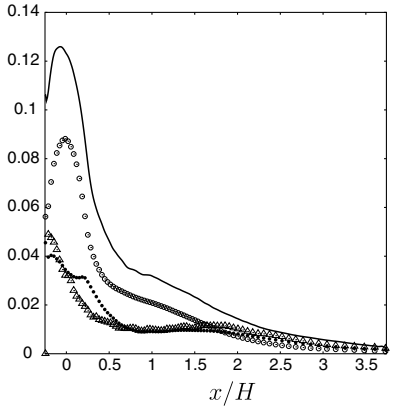

Fig. 15. Variance Ξ'^2 of the PDF of the concentration distribution along the main duct (solid); local mean variance at the centreline $\langle c'^2 \rangle$ (triangles); cross-sectional average of the LSV (circles) and SSV (black dots).

dency is visible in the local variance along the centreline (Fig. 15, symbols). In addition to this the local variance even increases slightly between $x/H = 0.5$ and $x/H = 2.0$ due to backmixing and the complex 3D structure of the flow and scalar fields.

The appearance of a bimodal PDF can be explained when looking at the production of small scale variance P_c, especially at $x/H = 1.25$ (Fig. 16). The production of SSV is high and positive in two, more or less distinct, areas. In these two areas large scale variance will be removed and, when comparing these areas with the mean scalar field, one will see that the mean concentration ranges from $c = 0.5$ to $c \approx 0.9$ in the one and from $c = 0.5$ to $c \approx 0.1$ in the other area. As the large scale turbulent mixing process is confined to these two spatially separated areas, unmixed fluid mixes with perfectly mixed fluid, thus producing these two distinct peaks in the PDFs. This leads to the observed flat slope in the development of the absolute variance of the scalar between $0.75 < x/H < 1.75$. It should also be noted that within this region the small scale variance (SSV) is almost constant, meaning that the production and dissipation of SSV are in equilibrium. When moving further down the duct, mixing by diffusion becomes dominant, the flatness of the PDFs decreases further and the peaks become more distinct ($x/H = 2.75$) and finally the peaks themselves move slowly towards the mean due to molecular diffusion ($x/H = 3.75$) as the flow starts to relaminarise.

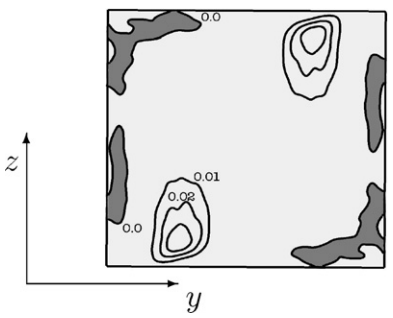

Fig. 16. P_c at $x/H = 1.25$.

4. Conclusions

In this paper we presented the results of a combined DNS and PIV study of the flow in a static CIJR configuration at $Re_b = 500$, with $Sc = 1$ in the simulation. The comparison between DNS and experiment are satisfying considering the uncertainties in exactly matching the boundary conditions. DNS as well as the experiment reveal the same features as (i) symmetry in the $(y/H, z/H = 0.0)$ plane, (ii) a dominating flow of one inflow in the offset planes at $(x/H, y/H, z/H = \pm 0.1875)$ which gives rise to the main vortex, and (iii) secondary vortices in the offset planes near the inflow of one jet.

We were able to demonstrate that the symmetry of the flow about the plane $y = 0$ is broken in the experiment as well as in the DNS. As opposed to previous studies (Wood et al., 1991; Telib et al., 2004) this feature can be observed in the DNS only when the feeding pipes are included in the simulation which was not the case in the previous studies. Reducing the computational effort by assuming symmetry must be avoided as it will provide a wrong flow field. To what extent this symmetry breaking is dependent on specific geometric attributes, such as the distance of the feeding tubes to their diameter H/D remains an open question.

The analysis of the DNS data of the flow field showed that three different zones can be distinguished. The *mixing zone* directly between the two feeding pipes where the main vortex develops due to a deflection of the inflow jets in opposite directions and a strong three-dimensional turbulent flow field with a axisymmetric turbulence structure. This is followed by a short *isotropic zone* where the mean flow field is stabilised by the main vortex and the turbulence is isotropic with still strong intensities. In the *relaminarisation zone* the turbulent intensities decrease rapidly, the rotation of the mean flow becomes more axisymmetrical and slows down, and the flow approaches a laminar duct flow.

The characteristics of the turbulence directly dominates the mixing of the two feeding streams. In the first two zones rapid mixing occurs by the strong three-dimensional turbulence with a fast approach to the form of a monomodal PDF of the scalar field in the cross-section at $x/H = 0.75$. Between $x/H = 0.75$ and $x/H = 1.25$ the reduction of scalar variance slows down, because the turbulent mixing concentrates in two spatially separated zones each containing fluid predominantly from one of the two feeding pipes. In these zones we observe that perfectly mixed fluid is mixed with unmixed fluid. This produces a bimodal PDF from the monomodal one that was already present shortly after the impingement of the jets. From $x/H = 2.0$ onward, the cross-sectional averaged SSV is larger than the LSV, and thus diffusion is the main mixing process as the flow slowly relaminarises due to the low Reynolds number.

An analysis of the large scale and small scale mixing times showed that the total mixing process is dominated by the large scale mixing. The data showed that the production of scalar variance becomes negative in some parts of the flow, thus removing small scale variance and producing large scale variance. This cannot be captured by standard eddy diffusivity models and leads to a poor definition of the large scale mixing times, when defining them on a local basis.

For predicting the mixing in confined impinging jet reactors this study demonstrated that (i) the flow model has to avoid symmetry assumptions and permit possible symmetry breaks, and (ii) the mixing model has to allow for complex changes of the shape of the scalar PDFs.

References

Baldyga, J., Bourne, J.R., 1999. Turbulent Mixing and Chemical Reactions. Wiley, Chichester.

Ferziger, J., Perić, M., 1997. Computational Methods for Fluid Dynamics, second ed. Springer, Berlin.

Fox, R.O., 2003. Computational Models for Turbulent Reacting Flows. Cambridge University Press.

Harlow, F.H., Welsh, J.E., 1965. Numerical calculation of time-dependent viscous incompressible flow with free surface. Phys. Fluids 8, 2182–2189.

Johansson, P., Andersson, H., 2005. Direct numerical simulation of two opposing wall jets. Phys. Fluids 17 (05).

Johansson, A., Wikström, P., 1999. DNS and modelling of passive scalar transport in turbulent channel flow with a focus on scalar dissipation rate modelling. Flow Turbul. Combust. 63, 233–245.

Johnson, B., Prud'homme, R., 2003. Chemical processing and micromixing in confined impingin jets. AIChE J. 49 (9), 2264–2282.

Kawamura, H., Ohsaka, K., Abe, H., Yamamoto, K., 1998. DNS of turbulent heat transfer in channel flow with low to medium-high Prandtl number fluid. Int. J. Heat Fluid Flow 19, 482–491.

Kolmogorov, A., 1941. The local structure of turbulence in incompressible viscous fluid for very large Reynolds numbers. Dokl. Acad. Nauk. SSSR 30 (301).

Le Duc, A., Peller, N., Manhart, M., Wachsmann, E.-P., 2005. Aerodynamics and acoustic sources of the exhaust jet in a car air-conditioning system. In: Rodi, W., Mulas, M. (Eds.), Proceedings of the ERCOFTAC International Symposium on Engineering Turbulence Modelling and Measurements, ETMM6. Elsevier, Amsterdam, pp. 709–718.

Liu, Y., Fox, R., 2006. CFD predictions for chemical processing in a confined impinging-jets reactor. AIChE J. 52 (2), 731–744.

Lumley, J.L., Newman, G., 1977. The return to isotropy of homogeneous turbulence. J. Fluid Mech. 82, 161–178.

Manhart, M., 2004. A zonal grid algorithm for DNS of turbulent boundary layers. Comput. Fluids 33 (3), 435–461.

Manhart, M., Tremblay, F., Friedrich, R., 2001. MGLET: a parallel code for efficient DNS and LES of complex geometries. In: Jensen, C.B. (Ed.), Parallel Computational Fluid Dynamics 2000. Elsevier Science BV, Amsterdam, pp. 449–456.

Peller, N., Le Duc, A., Tremblay, F., Manhart, M., 2006. High-order stable interpolations for immersed boundary methods. Int. J. Numer. Meth. Fluids 52 (11), 1175–1193.

Pope, S.B., 2000. Turbulent Flows. Cambridge University Press, Cambridge.

Roelands, M., Derksen, J., Horst, J., Kramer, H., Jansens, P., 2003. An analysis of mixing in a typical experimental setup to measure nucleation rates of precipitation processes. Chem. Eng. Technol. 26, 296–302.

Schwarzer, H.C., Schwertfirm, F., Manhart, M., Schmid, H.J., Peukert, W., 2006. Predictive simulation of nanoparticle precipitation based on the population balance equation. Chem. Eng. Sci. 61, 167–181.

Telib, H., Iollo, A., Manhart, M., 2004. Analysis and low order modeling of the inhomogeneous transitional flow inside a T-mixer. Phys. Fluids 16 (7), 2717–2731.

Tosun, G., 1987. A study of micromixing in tee mixers. Ind. Eng. Chem. Res. 26, 1184–1193.

Tremblay, F., Manhart, M., Friedrich, R., 2001. DNS and LES of flow around a circular cylinder at a subcritical Reynolds number with cartesian grids. In: Friedrich, R., Rodi, W. (Eds.), LES of Complex Transitional and Turbulent Flows. Kluwer Academic Publishers, Dordrecht, pp. 133–150.

Unger, D., Muzzio, F., 1999. Laser-induced fluorescence technique for the quantification of mixing in impinging jets. AIChE J. 45 (12), 2477–2486.

Williamson, J.H., 1980. Low-storage Runge–Kutta schemes. J. Comput. Phys. 35 (48), 48–56.

Wood, P., Hyrmak, A., Yeo, R., Johnson, D.A.T., 1991. Experimental and computational studies of the fluid mechanics in an opposed jet mixing head. Phys. Fluids 3, 1362–1368.